Analysis of Synoptic Disturbance in Maritime Continent Using Spherical Harmonics Transformation Method

Sayful Amri[1,2], Faiz Rohman Fajary[3], Tri Wahyu Hadi[3]

[1]Earth Sciences Study Program, Faculty of Earth Sciences and Technology, Institut Teknologi Bandung, Bandung, Indonesia, 40132
[2]Tegal Meteorological Station, Indonesian Agency for Meteorology Climatology and Geophysics (BMKG), Tegal, Indonesia, 52113
[3]Atmospheric Sciences Research Group, Faculty of Earth Sciences and Technology, Institut Teknologi Bandung, Bandung, Indonesia, 40132

ABSTRACT

This study aims to modify the idea of WK99-analyzing the existence of signature in wavenumber and frequency spectrum when the analyzed Outgoing Longwave Radiation (OLR) data is associated with a unique phenomenon in Maritime Continent (MC), Borneo vortex (BV). Although BV is often related to easterly equatorial wave disturbances, there was no specific study to examine its behavior in the spectral domain. The purpose of this study is to develop a method to diagnose certain signatures of BV through spectrum analysis of OLR data when BV occurs. In contrast to previous studies, to present the unique phenomenon in MC as a target for diagnostics, spectrum analysis was performed by Spherical Harmonics (SH). This method used trigonometric and associated Legendre functions which present zonal and meridional structure, respectively. Hence, the separation of antisymmetric and symmetric patterns to the equator in this method was considered better than WK99. The results showed that the spectral signatures of BV were characterized by enhancements of westward propagating mixed Rossby gravity (MRG) with zonal wavenumbers of 5-10 and frequencies of 0.12-0.2 cycle per day (cpd) (periods of 5-8 days). Moreover, the spectrum of the wave is getting stronger for longer BV duration.

KEYWORDS
Borneo vortex, equatorial waves, mixed Rossby gravity, spectrum analysis, spherical harmonics

INTRODUCTION

Atmospheric dynamics are formed by three main movements, namely average flow, waves, and turbulence. In the middle latitude region, the synoptic weather pattern is strongly influenced by the dynamics of the Rossby wave (e.g. Röthlisberger et al., 2019; Shi et al., 2016; Swenson and Straus, 2017; Zschenderlein et al., 2018). On other hand, synoptic weather in tropics was influenced by various types of equatorial waves (e.g. Fukutomi et al., 2016; Fukutomi, 2019; Kim et al., 2019; Matsuno, 1966; Yang et al., 2018), which theoretically include Kelvin waves, equatorial Rossby (ER), westward inertia-gravity (WIG), eastward inertia-gravity (EIG) and mixed Rossby gravity (MRG) (Matsuno, 1966).

In brief, the Kelvin wave is a wave that spreads at the equator from west to east due to the Coriolis force (Matsuno, 1966). ER waves are equatorial planetary waves (very long 4,000-10,000 km) that propagate westward (Kiladis et al., 2009). Many efforts have been performed to study atmospheric dynamics to seek interaction between various waves and atmosphere. Several equatorial planetary waves propagate westward: very long wave ER, cloud cluster disturbance WIG associated with Madden-Julian Oscillation (MJO), and convectively active waves that can evolve into the

synoptic disturbance MRG (Kiladis et al., 2009). EIG waves are similar to MRG but propagate eastward, instead.

Equatorial waves influence atmospheric oscillations on pressure, air temperature, humidity, convection, and wind, in which the more magnitude oscillations can directly affect weather in the tropics (Ling et al., 2019; Türkeş and Erlat, 2018; Ying and Zhang, 2017), such as the intensity and onset of precipitation in the tropics (Cavalcanti et al., 2017; Dias et al., 2018; Kim and Kim, 2016; Lubis and Jacobi, 2015; Niang et al., 2017; Sakaeda et al., 2020; Steptoe et al., 2018; Xie et al., 2017; Zhang et al., 2018). Equatorial waves theory developed by Matsuno (1966) has only been confirmed by Wheeler and Kiladis (1999) as WK99. This theory is used to analyze the spectrum of wavenumber-frequency from long-term Outgoing Longwave Radiation (OLR) data (~18 years).

The WK99 analysis method generally generates signatures from the existence of various types of equatorial waves, which are then used as filters to get the characteristic of wave structures spatially and temporally (Ogrosky and Stechmann, 2016). Wu et al. (2015a, 2015b) applied the WK99 method to study the evolution of the structure of westward-propagating tropical waves (WTWs) under different monsoon trough (MT) conditions in Western North Pacific (WNP). In their study, they identified a certain spectrum as signatures of the MT phenomenon, but the analysis was limited only to WTWs in the WNP region.

Their approach to identify a certain spectrum may be promising to be applied for diagnosing other atmospheric phenomena in tropics. Here, we will apply the approach to diagnose unique phenomena in the Maritime Continent (MC) and its relationship to the dynamics of the global atmosphere. For a case study, Borneo Vortex (BV) is selected as representative of the MC (Dang-Quang et al., 2016). Hardly any studies have been performed to analyze BV in the spectral domain.

The WK99 method is the most popular space-time spectral analysis (STSA) method in the field (Raghavendra et al., 2019), but this method has a shortcoming to describe the global convective pattern as its OLR data domain is limited to the tropics (Ayuliana et al., 2019). To tackle this limitation, an alternative STSA method for spectral analysis of wavenumber-frequency to global OLR data has been proposed based on spherical harmonics (SH) transformations (Ayuliana et al., 2019). The SH function consists of trigonometric and associated Legendre functions, which present zonal and meridional structures, respectively. Global OLR data, which is the function of space on the spherical surface can be represented by the SH function. In general, the OLR power spectrum obtained from the SH

method can capture more planetary waves than the WK99 method (Ayuliana et al., 2019). Two reasons may support this claim, including the SH method use global OLR data, therefore it can identify convection patterns that propagate on the zonal direction and that vary towards meridional widely.

Furthermore, in the equator, the separation of antisymmetric and symmetric patterns in the SH transformation method was more appropriate than WK99, because it was based on associated Legendre polynomials (Ayuliana et al., 2019). Therefore, this research aims to develop a BV diagnostic method in the spectral domain and to analyze the relationship between BV and equatorial waves.

RESEARCH METHODS

This study applied two approaches to determine BV signatures on the spectral domain, namely by (i) determining the timing of BV events and (ii) analyzing BV signatures on the wavenumber-frequency spectrum.

Data and Sources

The data used in this study were global horizontal wind (u and v) data from the 925 hPa level and global OLR data. Wind data with a spatial resolution of 2.5° and a 6-hour temporal resolution were obtained from the ERA-Interim reanalysis and provided by the European Center Medium-Range Weather Forecast (ECMWF). The data is available online at http://apps.ecmwf.int/datasets/data/interim-full-daily/. Secondly, interpolated global OLR data at daily resolution with a spatial resolution of 2.5° was provided by NOAA (Liebmann and Smith, 1996). The OLR data is available online at https: //www.esrl.NOAA/gov/PSD/. We used data from 1988-2018 (30 years) for the period November-December-January-February-March (NDJFM).

Determination of Times of BV Events

To obtain the occurrence of BV, we visually identified the streamline of u and v on the level of 925 hPa at 00 UTC in the NDJFM period (Chang et al., 2005, 2016). BV was identified if there is a closed counterclockwise cyclonic circulation in the BV region, and at least one wind speed was recorded more than 2 ms^{-1} at the corner of the 2.5° x 2.5° grid box, where the center of the cyclonic circulation is located. In this study, the BV region was at the coordinate of 105°E-117.5°E and 2.5°S-7.5°N (Figure 1a), which was a combination of BV study areas by Chang et al. (2005) and Juneng and Tangang (2010). An example of BV identification in this study is presented in Figure 1b. After all BV events were identified, the times of BV events were obtained during the study period.
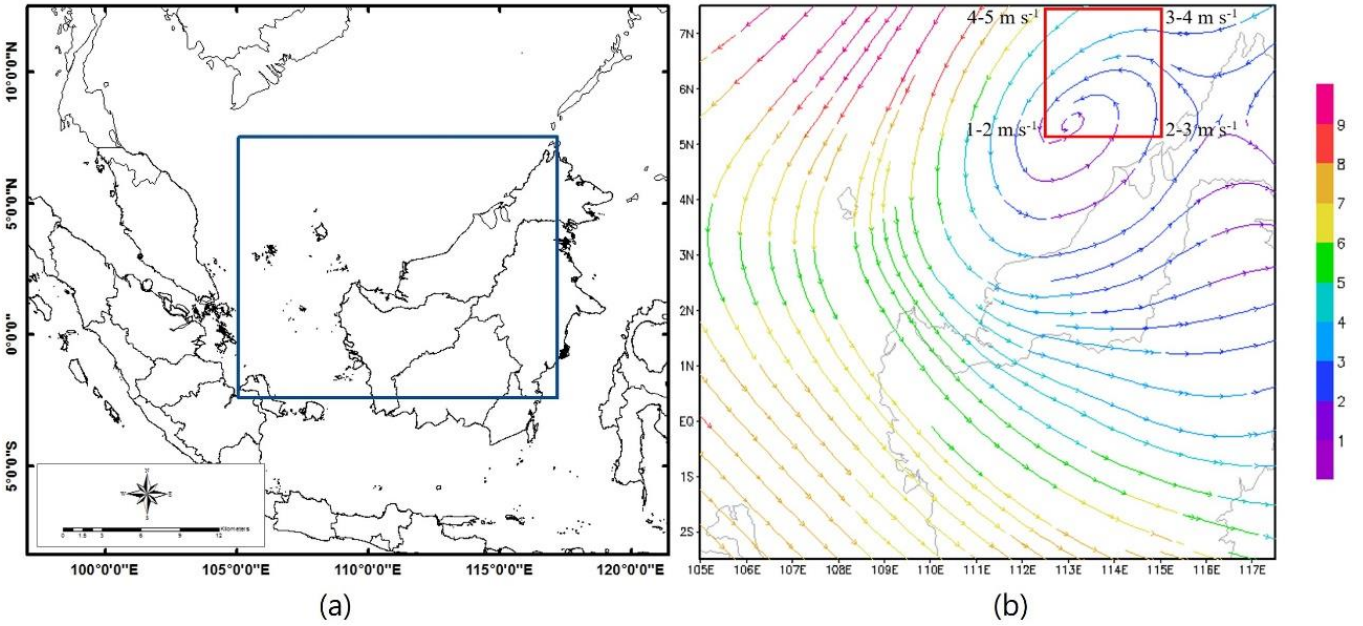
Figure 1. (a) Region of BV in this study is a region bound by 105°E-117.5°E and 2.5°S-7.5°N (blue box) which is a combination between the region of BV by Chang et al. (2005) and Juneng and Tangang (2010). (b) Example of BV identification dated November 25, 1988-hour 00 UTC (07 WIB). Streamline color shows speed (in ms^{-1}). A red box shows the location of the vortex center at 2.5° resolution.

Signatures of BV on the Wavenumber-Frequency Spectrum

In general, the analysis of BV signatures in the spectral domain consists of three main stages. First, the initial analysis of OLR data was carried out before applying the STSA. The analysis included removal of the average and the first three harmonics from the annual cycle of each grid (periods of one year, six months, and four months), and then the global OLR anomaly data was obtained [$OLR(\theta, \lambda, t)$]. Furthermore, the OLR anomaly data was cut into several segments for all BV events, no BV event (noBV), and BV groups with different duration (BV with duration 1-3 days [BV 1-3 days], BV with duration 4-7 days [BV 4-7 days], and BV with a duration of more than 7 days). The length in 1 segment is 31 days, which is ± 15 days for the first day (H0) for all BV events and BV groups with different duration and +30 days for H0 for each noBV event.

Secondly, the SH analysis was applied to each of the global OLR anomaly data segments [$OLR(\theta, \lambda, t)$] to obtain the real and imaginary coefficients [$OLR_n^m(t)$] of the SH basis functions [$Y_n^m(\lambda, \mu)$] for all occurrences of BV, noBV, and BV groups with different duration. The SH analysis in this study used the *shaec* function available from SH packages in the NCAR command language (NCL). Generally, the SH analysis of each of the global OLR anomaly data segments [$OLR(\theta, \lambda, t)$] can be expressed by Equation (1).

$$OLR\ (\theta, \lambda, t) = \sum_m \sum_n OLR_n^m(t) Y_n^m(\lambda, \mu) \qquad (1)$$

$OLR(\theta, \lambda, t)$ is OLR anomaly data segment (θ, λ, and t function), $OLR_n^m(t)$ is real and imaginary coeffi-

cients of the SH basis function in each OLR anomaly data segment (m, n, and t function), $Y_n^m(\lambda, \mu)$ is SH basis function, θ is latitude, λ is longitude, m is zonal wavenumber (number of waves along the latitude circle), n is 2-dimensional wave number (total), and t represents time.

Third, the Fast Fourier Transform (FFT) was applied to the time series of real and imaginary coefficients of the SH basis function to obtain the wavenumber-frequency spectrum (m, n, and f function) in each segment when all occurrences of BV, noBV, and BV groups with different duration. Then, we average the power spectrum in each segment for all occurrences of BV, noBV, and BV groups with different duration. We categorized the average power spectrum into three power spectrums, namely the antisymmetric, symmetric, and global power spectrum (background spectrum). The antisymmetric (symmetric) power spectrum was obtained from the average of zonal wavenumber (m) for all odd (even) [n-m], and the global power spectrum was obtained from the average m for all 2-dimensional wave number (n).

The criteria of the wavenumber and frequency that are identified as BV signatures in this study were similar to the previous study approach (Wu et al., 2015a), namely the differences that appear consistently in the comparison between the ratio of the power spectrum when BV occurs with noBV, as well as when BV occurs with the different duration. Therefore, we compared the ratio of the BV antisymmetric (symmetric) spectrum on the noBV global spectrum with the ratio of the noBV antisymmetric (symmetric) spectrum on

the noBV global spectrum. The two power spectrum ratios were compared to find the differences in the wave spectrum when BV and noBV occurs. Then we calculated the ratio of the antisymmetric (symmetric) power spectrum between groups of BV with the different duration on the noBV global spectrum. This ratio then compared to examine the differences of consistently wave spectrum along with a longer BV duration.

OLR anomaly data was filtered and reconstructed based on wavenumbers and frequencies that identified as BV signatures in the spectral domain. Before the two processes were carried out, we implemented the similar procedure to obtain the power spectrum on the global OLR data. Furthermore, the real and imaginary coefficients of the SH basis function (m, n, and f function) were filtered using zonal wavenumbers and frequencies that were identified as BV signatures. Then, we applied the Inverse Fast Fourier Transform (IFFT) to the coefficients, resulting in the filtered time series coefficients of SH basis functions [$OLR_n^m(t)$]. We reconstructed the OLR anomaly data by applying the SH synthesis on the filtered time series coefficients of SH basis functions, and we call it a new OLR anomaly data [$OLR(\theta, \lambda, t)$]. The SH synthesis in this study was calculated by the *shsec* function in the NCL SH package.

The new OLR anomaly data was used to analyze the relationship between equatorial waves and BV. First, the variance of the OLR anomaly data, which has been filtered during the BV event was calculated to analyze the distribution of the equatorial wave energy at the time of the BV event. Secondly, we visually compared the variance patterns of the OLR anomaly data between BV events and noBV events. This comparison will confirm BV signatures in the spectral domain as well as in the physical domain.

RESULTS AND DISCUSSIONS

Comparison of OLR Spectrum During BV and noBV Events

The results showed that there were 506 BV events during the NDJFM period from 1988-2018. The events consisted of 402 events with a life span of 1-3 days, 86 events with a life span of 4-7 days, and 18 events with a life span of more than 7 days. From this BV identified, we analyzed the wavenumber-frequency spectrum during BV and noBV events. Our results indicated that during BV events, the wave spectrum of Kelvin was wider, stronger, and more uniform than that of noBV events.

The results were shown by the ratio of the BV antisymmetric spectrum on the noBV global spectrum (Figure 2a) and the ratio of the BV antisymmetric spectrum on the noBV global spectrum (Figure 2b). A distinct difference was shown in the spectrum of west-

ward-propagating tropical waves (WTWs). For instance, during the BV events, the MRG wave was wider and stronger than noBV events, especially in zonal wavenumbers of 5-0 and frequencies of 0.12-0.2 cpd (periods of 5-8 days).

Figure 2c-d shows that symmetric components of equatorial waves have some differences with antisymmetric components (Figure 2a-b). Although the wave spectrum of Kelvin during BV events was wider and more uniform than that of noBV events, it was weaker for low frequencies (Figure 2c-d). The wave spectrum of ER was equally distributed during BV events at an equivalent depth of 12, whereas it was wider during noBV events at an equivalent depth of 50. The symmetric wave spectrum of MRG during BV events was stronger and more uniform than that of noBV events. This can be considered as a specific signature of the OLR wave spectrum when BV events. This finding contradicted the previous research using WK99, which explained the symmetric component of the MRG wave was not visible (Wheeler and Kiladis, 1999).

Furthermore, the wave spectrum of WIG during BV events was stronger than that of noBV events, especially at a zonal wavenumber of 7-13 and frequencies of 0.38-0.5 cpd (equivalent depths of 12 and 25). This pattern was also identified in the wave spectrum of EIG when BV occurs was stronger than noBV events. This may indicate that the inertia gravity wave might have formed due to the convective activity of BV. The results were shown by the ratio of the BV symmetric spectrum on the noBV global spectrum (Figure 2c) and the ratio of the noBV symmetric spectrum on the noBV global spectrum (Figure 2d).

Comparison of OLR Spectrum when BV Occurs with Different Durations

BV events with different duration influence the dynamic of the OLR spectrum. For the antisymmetric spectrum, the wave spectrum of MRG seems stronger and wider when BV 4-7 days (Figure 3b) than BV 1-3 days (Figure 3a), in particular for zonal wavenumbers of 1-7 and periods of 4-8 days. However, the wave spectrum of MRG when BV with duration more than 7 days (Figure 3c) is weaker than BV 4-7 days (Figure 3b), inparticular for zonal wavenumbers of 3 and 7 and periods of 4-8 days.

In general, the wave spectrums of Kelvin and EIG when BV 4-7 days (Figure 3b) and BV with a duration of more than 7 days (Figure 3c) are weaker than the spectrums of the two waves when BV 1-3 days (Figure 3a). Therefore, the strengthening of the wave antisymmetric spectrums of Kelvin and EIG when BV occurs (Figure 2a) compared to the noBV event (Figure 2b) does not appear to be consistent when when BV occurs with a longer duration (Figure 3a-c).
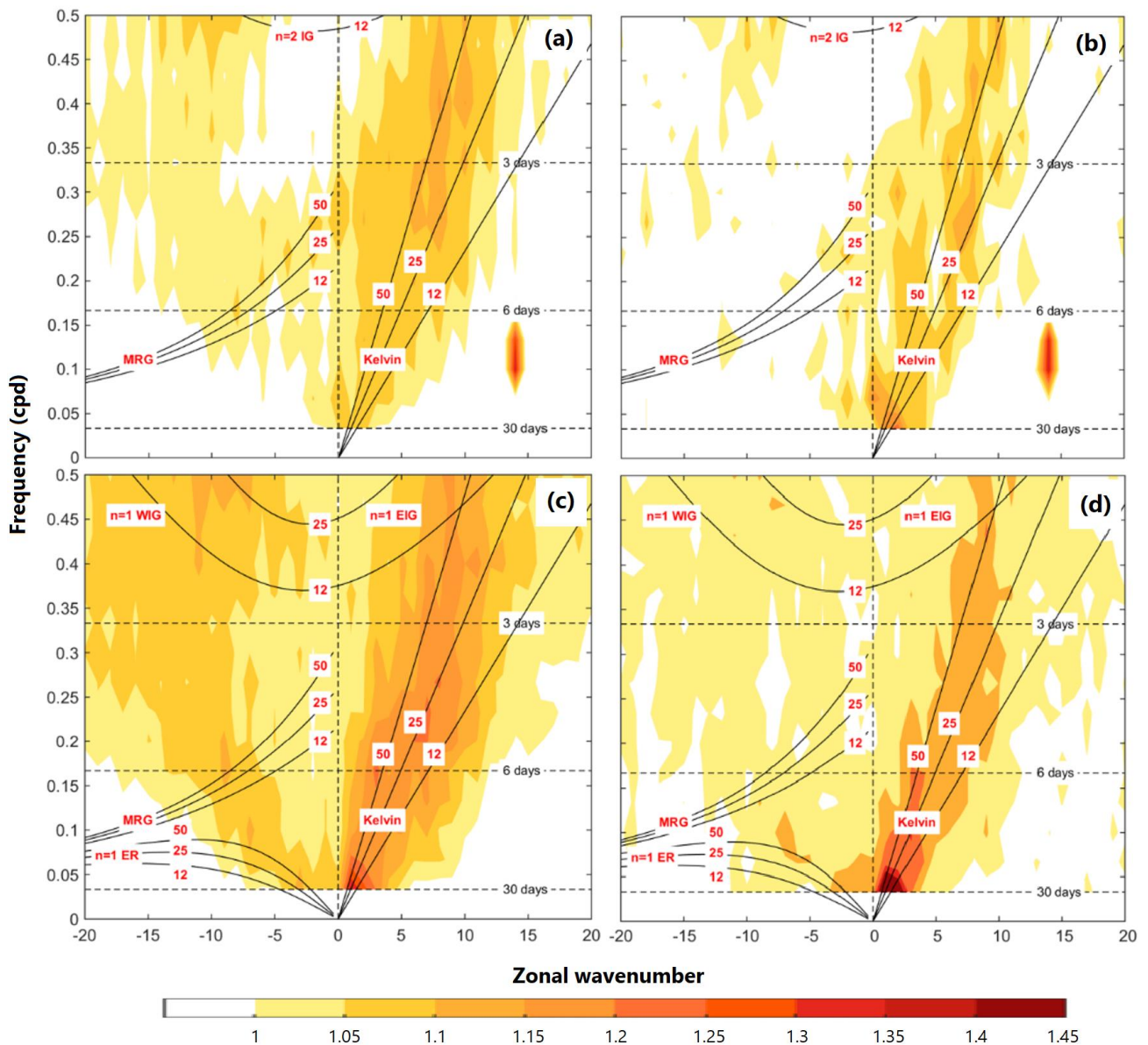
Figure 2. (a) Ratio of the BV antisymmetric spectrum (during all BV events) on the noBV global spectrum; (b) ratio of the noBV antisymmetric spectrum on the noBV global spectrum; (c) ratio of the BV symmetric spectrum on the noBV global spectrum; and (d) ratio of the noBV symmetric spectrum on the noBV global spectrum. Superimposed are the dispersion curves of the equatorial waves (black curves) for the three equivalent depths of h = 12, 25, and 50 (red numbers).

On the other hand, when we analyzed the symmetric spectrum, the longer duration of the BV events will cause the three waves of MRG, Kelvin, and WIG were wider and stronger (Figure 3d-f). This may be related to the greater convection activity when BV lasts longer. The wave spectrum of Kelvin when BV with a duration of more than 7 days seems stronger than BV 1-3 days and BV 4-7 days. However, the wave spectrum of Kelvin when BV 4-7 days (Figure 3e) is generally weaker than BV 1-3 days (Figure 3d). The pattern is also seen in the two wave spectrums of EIG and WIG. Therefore, the strengthening of the three symmetric wave spectrums of Kelvin, EIG, and WIG when BV occurs (Figure 2c) compared to the noBV event (Figure 2d)

does not appear to be consistent when BV occurs with a longer duration (Figure 3d-f).

Wavenumber and Frequency Filtering

Then we analyzed wavenumber and frequency filtering on OLR data. The finding showed consistent differences in the strengthening of the MRG wave spectrum both for symmetric and antisymmetric components when we compared BV and noBV events. The difference was clearly shown in the zonal wavenumbers of 5-10 and frequencies of 0.12-0.2 cpd (periods of 5-8 days). Therefore, OLR data was filtered based on these wavenumbers and frequencies (Figure 4). This was done to confirm the BV signatures in the spectral domain that was proven in the physical domain. In this study, filter-
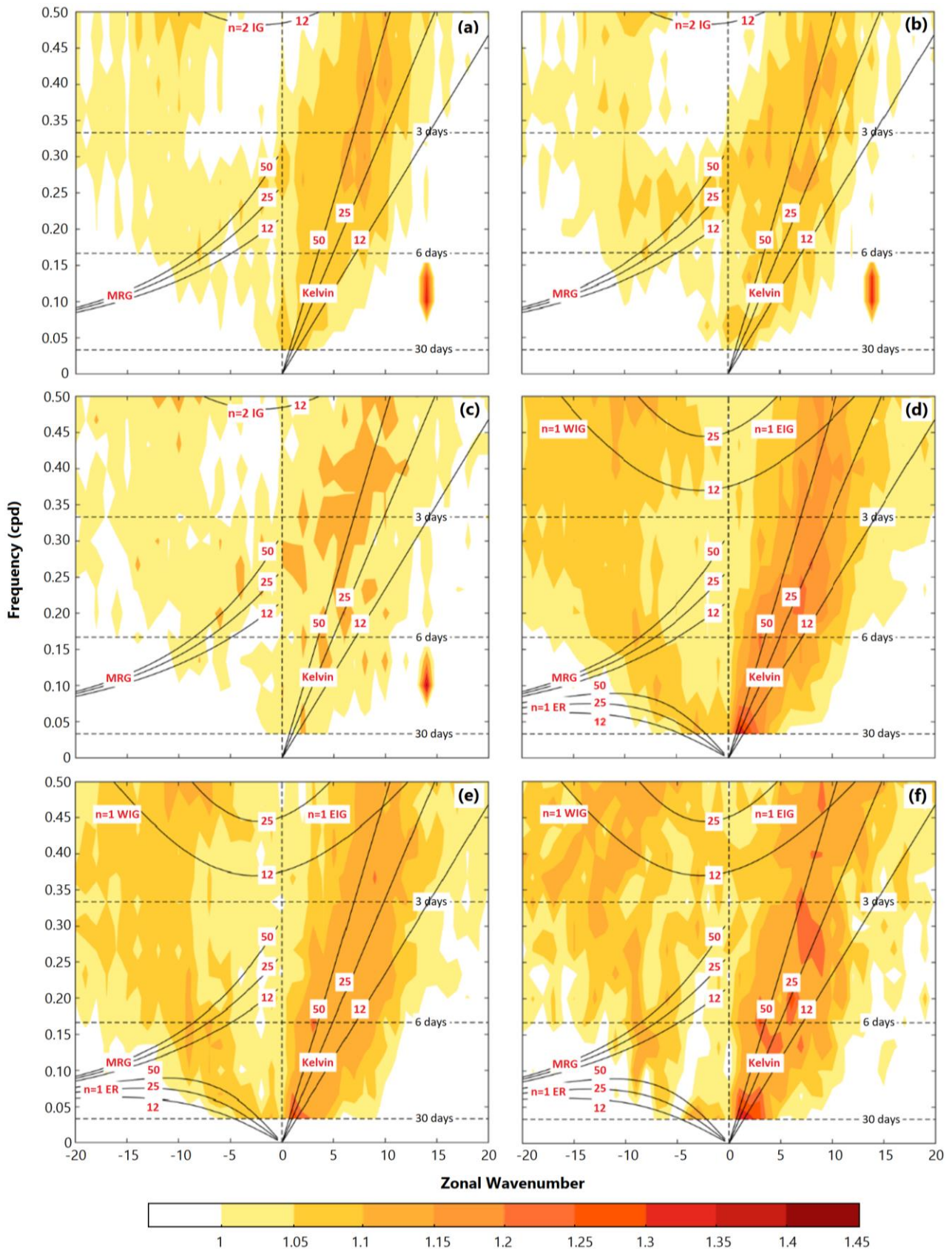
Figure 3. (a) Ratio of the BV 1-3 days antisymmetric spectrum on the noBV global spectrum; (b) ratio of the BV 4-7 days antisymmetric spectrum on the noBV global spectrum; (c) ratio of the antisymmetric spectrum during BV with a duration of more than 7 days on the noBV global spectrum; (d) ratio of the BV 1-3 days symmetric spectrum on the noBV global spectrum; (e) Ratio of the BV 4-7 days symmetric spectrum on the noBV global spectrum; and (f) ratio of the symmetric spectrum during BV with a duration of more than 7 days on the noBV global spectrum. Superimposed are the dispersion curves of the equatorial waves (black curves) for the three equivalent depths of h = 12, 25, and 50 (red numbers).
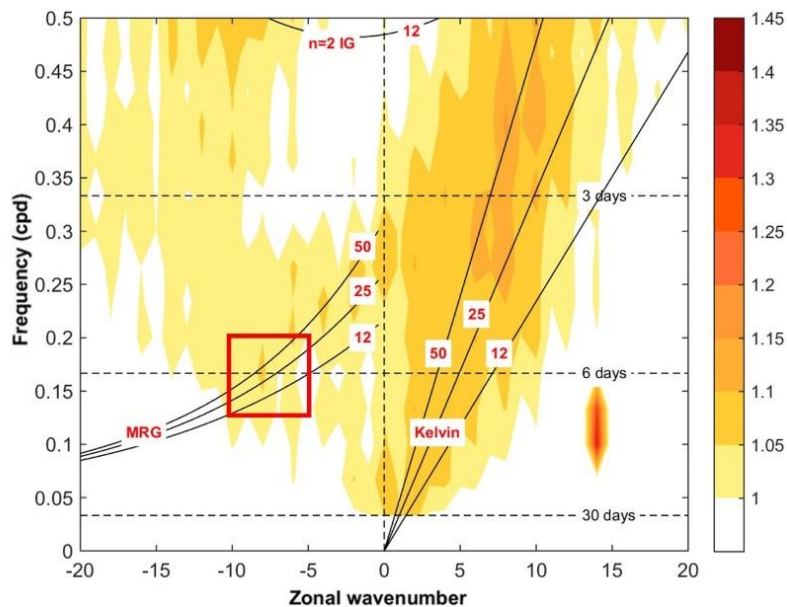
Figure 4. The domain of zonal wavenumber and frequency was used (red color boxes) on filtering and reconstruction of the coefficient SH basic function (*m*, *n*, and *f* function) to the physical domain (*ϑ*, *λ*, and *t* function).

ing and reconstruction were carried out only on the antisymmetric component, because the nature of the MRG waves was more dominant in the antisymmetric component.

We took an example of the BV events on 11 December 1996 - 26 December 1996 (Figure 5) to show the impact of filtered MRG waves. It was clearly shown that the MRG wave was strong especially at the beginning of BV formation (Figure 5a). On the first day of the event, the OLR anomaly was strong negative (convection) that allowed MRG to enter the BV area. Then the MRG wave was weaker in the following days. This indicates that the possibility of BV formation can be also influenced by the presence of convection from the MRG wave.

Finally, we analyzed the spatial patterns of the filtered OLR anomaly based on their variance values during BV events (Figure 6a) and noBV events (Figure 6b). The patterns were analyzed to confirm the formation of BV signatures in the spectrum and physical domains. This variance value was equivalent to the magnitude of the energy distribution of the filtered equatorial wave (MRG). The comparison results are matching the results obtained from the previous spectrum domain, in which the energy distribution of the MRG wave at the BV events was stronger than at noBV events.

Some types of Equatorial waves are known can trigger vortex, TD, and TC formation in several TC basins in the world (Ching et al., 2015; Wu and Takahashi, 2018). BV may be also related to equatorial wave dynamics, but there are no studies that comprehensively examine BV in the spectral domain. This study analyzes the phenomenon of BV based on space-time spectral analysis by the combination of SH (Ayuliana et al., 2019) and Fourier transformation methods to obtain the spectrum of wavenumber-frequency from global OLR anomaly data. Thus, this study is different from other space-time spectral analysis, which generally uses the WK99 method.

In general, the OLR power spectrum obtained from the SH method can capture more planetary waves than the WK99 method (Ayuliana et al., 2019). In this study, the method of BV identification is referred to by Chang et al. (2005). During the thirty East Asian winters of 1988-2018, there were 506 BV events, which are 402 events with a life span of 1-3 days, 86 events with a life span of 4-7 days, and 18 events with a life span of more than 7 days. The spectrum of OLR anomaly data shows that the wave spectrum of MRG seems stronger when BV exists than noBV (m = 5-10 and T = 5-8 days (f = 0.12-0.2 cpd)). We identified the strengthening of the MRG wave spectrum as a signature of BV because it is consistent with the longer duration of the BV, which the other types of Equatorial waves are not.

In this study, the space-time spectral analysis was only applied to the OLR anomaly data, therefore it has not fully proven the effect of equatorial waves on BV events. Further research needs to be done by involving the analysis of wind data and other data that more directly represent the presence and interaction of equatorial waves, as well as the possibility of atmospheric dynamics interactions between the tropics and extra-tropics.

CONCLUSIONS

This study examined the BV phenomenon based on space-time spectral analysis using the spherical harmonics (SH) transformation method. Several findings are summarized as follows:
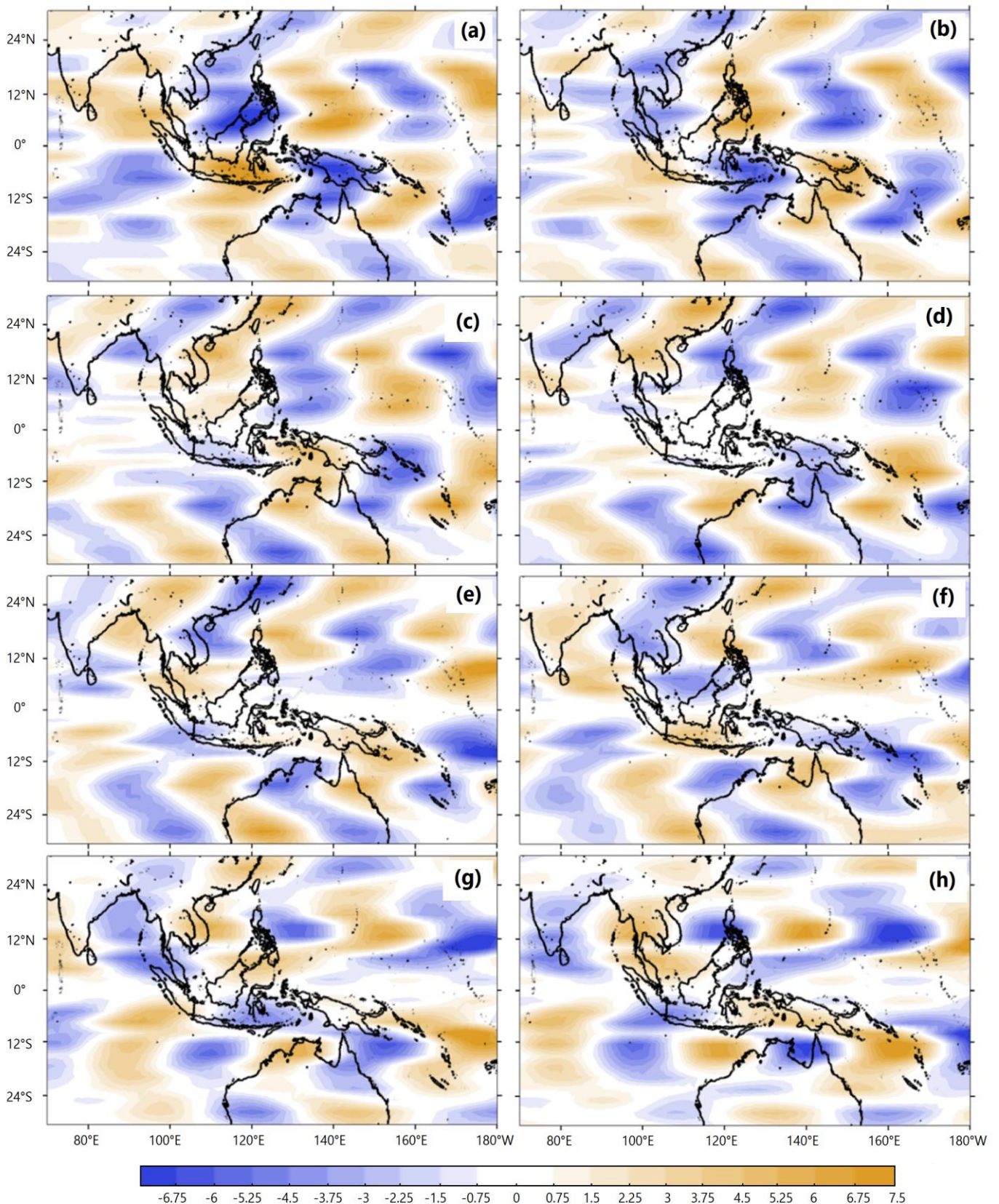1. During the period 1988-2018, between November

Figure 5. OLR anomalies that have been filtered in the time of BV from 11-26 December 1996 based on zonal wavenumbers and frequencies that become the signature of BV. (a)1st day of BV; (b)3rd day of BV; (c)5th day of BV (d)7th day of BV; (e)9th day of BV; (f)11th day of BV; (g)13th day of BV; (h)15th day of BV.

to March (NDJFM), 506 BV events were identified, namely, 402 events with a life span of 1-3 days, 86 events with a life span of 4-7 days and 18 events with a life span more than 7 days.

2. The composite spectrum from OLR anomaly data shows an amplified amplitude of MRG wave (anti-symmetric and symmetric) with zonal wavenumbers of 5-10 and frequencies of 0.12-0.2 cpd (periods of
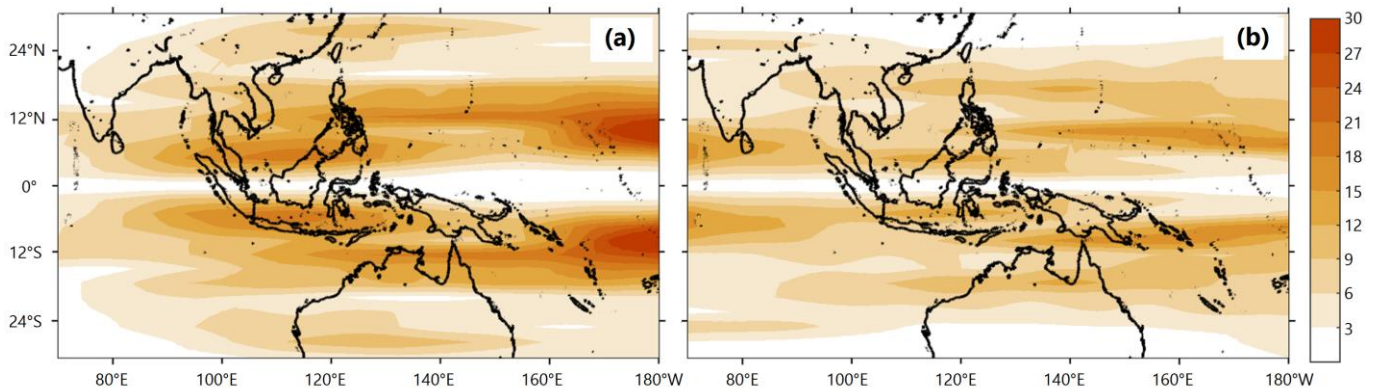
Figure 6. (a) Composite of filtered OLR anomaly variance of MRG waves during all BV events. (b) Composite of filtered OLR anomaly variance of MRG waves during noBV events.

5-8 days). We identified the strengthening of the MRG wave spectrum as BV signatures because it is consistent with the longer duration of the BV, which the other types of Equatorial waves are not.

REFERENCES

Ayuliana, S., Fajary, F.R., Hadi, T.W., 2019. Space-Time Spectral Analysis of 2-D Signal on the Globe Using Spherical Harmonics and Wavelet Transform Methods. Presented at the Journal of Physics: Conference Series, IOP Publishing, p. 012088.

Cavalcanti, I.F. de A., Marengo, J.A., Alves, L.M., Costa, D.F., 2017. On the opposite relation between extreme precipitation over west Amazon and southeastern Brazil: observations and model simulations. International Journal of climatology 37, 3606–3618.

Chang, C.-P., Harr, P.A., Chen, H.-J., 2005. Synoptic Disturbances over the Equatorial South China Sea and Western Maritime Continent during Boreal Winter. Monthly Weather Review 133, 489–503. https://doi.org/10.1175/MWR-2868.1

Chang, C.-P., Lu, M.-M., Lim, H., 2016. Monsoon Convection in the Maritime Continent: Interaction of Large-Scale Motion and Complex Terrain. Meteorological Monographs 56, 6.1-6.29. doi:10.1175/AMSMONOGRAPHS-D-15-0011.1

Ching, L., Sui, C.-H., Yang, M.-J., Lin, P.-L., 2015. A modeling study on the effects of MJO and equatorial Rossby waves on tropical cyclone genesis over the western North Pacific in June 2004. Dynamics of Atmospheres and Oceans 72,70–87. doi:10.1016/j.dynatmoce.2015.10.002

Dang-Quang, N., Renwick, J., McGregor, J., 2016. On the Presence of Tropical Vortices over the Southeast Asian Sea–Maritime Continent Region. Journal of Climate 29, 4793–4800. https://doi.org/10.1175/JCLI-D-14-00468.1

Dias, J., Gehne, M., Kiladis, G.N., Sakaeda, N., Bechtold, P., Haiden, T., 2018. Equatorial Waves and the Skill of NCEP and ECMWF Numerical Weather Prediction Systems. Mon. Wea. Rev. 146, 1763–1784. doi:10.1175/MWR-D-17-0362.1

Fukutomi, Y., 2019. Tropical Synoptic-Scale Waves Propagating Across the Maritime Continent and Northern Australia. J. Geophys. Res. Atmos. 124, 7665–7682. https://doi.org/10.1029/2018JD029795

Fukutomi, Y., Kodama, C., Yamada, Y., Noda, A.T., Satoh, M., 2016. Tropical synoptic-scale wave disturbances over the western Pacific simulated by a global cloud-system resolving model. Theor Appl Climatol 124, 737–755. https://doi.org/10.1007/s00704-015-1456-4

Juneng, L., Tangang, F.T., 2010. Long-term trends of winter monsoon synoptic circulations over the maritime continent: 1962–2007. Atmospheric Science Letters 11, 199–203.

Kiladis, G.N., Wheeler, M.C., Haertel, P.T., Straub, K.H., Roundy, P.E., 2009. Convectively coupled equatorial waves. Reviews of Geophysics 47. https://doi.org/10.1029/2008RG000266

Kim, J., Kim, K.-Y., 2016. The tropospheric biennial oscillation defined by a biennial mode of sea

surface temperature and its impact on the atmospheric circulation and precipitation in the tropical eastern Indo-western Pacific region. Clim Dyn 47, 2601–2615. https://doi.org/10.1007/s00382-016-2987-9

Kim, Y.-H., Kiladis, G.N., Albers, J.R., Dias, J., Fujiwara, M., Anstey, J.A., Song, I.-S., Wright, C.J., Kawatani, Y., Lott, F., Yoo, C., 2019. Comparison of equatorial wave activity in the tropical tropopause layer and stratosphere represented in reanalyses. Atmos. Chem. Phys. 19, 10027–10050. https://doi.org/10.5194/acp-19-10027-2019

Liebmann, B., Smith, C.A., 1996. Description of a Complete (Interpolated) Outgoing Longwave Radiation Dataset.

Ling, J., Zhang, C., Joyce, R., Xie, P., Chen, G., 2019. Possible Role of the Diurnal Cycle in Land Convection in the Barrier Effect on the MJO by the Maritime Continent. Geophysical Research Letters 46, 3001–3011. https://doi.org/10.1029/2019GL081962

Lubis, S.W., Jacobi, C., 2015. The modulating influence of convectively coupled equatorial waves (CCEWs) on the variability of tropical precipitation. International Journal of Climatology 35, 1465–1483.

Matsuno, T., 1966. Quasi-Geostrophic Motions in the Equatorial Area. Journal of the Meteorological Society of Japan. Ser. II 44, 25–43. https://doi.org/10.2151/jmsj1965.44.1_25

Niang, C., Mohino, E., Gaye, A.T., Omotosho, J.B., 2017. Impact of the Madden Julian Oscillation on the summer West African monsoon in AMIP simulations. Clim Dyn 48, 2297–2314. https://doi.org/10.1007/s00382-016-3206-4

Ogrosky, H.R., Stechmann, S.N., 2016. Identifying Convectively Coupled Equatorial Waves Using Theoretical Wave Eigenvectors. Monthly Weather Review 144, 2235–2264. https://doi.org/10.1175/MWR-D-15-0292.1

Raghavendra, A., Roundy, P.E., Zhou, L., 2019. Trends in Tropical Wave Activity from the 1980s to 2016. Journal of Climate 32, 1661–1676. https://doi.org/10.1175/JCLI-D-18-0225.1

Röthlisberger, M., Frossard, L., Bosart, L.F., Keyser, D., Martius, O., 2019. Recurrent Synoptic-Scale Rossby Wave Patterns and Their Effect on the Persistence of Cold and Hot Spells. Journal of Climate 32, 3207–3226. https://doi.org/10.1175/JCLI-D-18-0664.1

Sakaeda, N., Kiladis, G., Dias, J., 2020. The Diurnal Cycle of Rainfall and the Convectively Coupled Equatorial Waves over the Maritime Continent.

Journal of Climate 33, 3307–3331. https://doi.org/10.1175/JCLI-D-19-0043.1

Shi, N., Wang, X., Zhang, L., Xu, H., 2016. Features of Rossby Wave Propagation Associated with the Evolution of Summertime Blocking Highs with Different Configurations over Northeast Asia. Monthly Weather Review 144, 2531–2546. https://doi.org/10.1175/MWR-D-15-0369.1

Steptoe, H., Jones, S., Fox, H., 2018. Correlations between extreme atmospheric hazards and global teleconnections: implications for multihazard resilience. Reviews of Geophysics 56, 50–78.

Swenson, E.T., Straus, D.M., 2017. Rossby Wave Breaking and Transient Eddy Forcing during Euro-Atlantic Circulation Regimes. Journal of the Atmospheric Sciences 74, 1735–1755. https://doi.org/10.1175/JAS-D-16-0263.1

Türkeş, M., Erlat, E., 2018. Variability and trends in record air temperature events of Turkey and their associations with atmospheric oscillations and anomalous circulation patterns. International Journal of Climatology 38, 5182–5204. https://doi.org/10.1002/joc.5720

Wheeler, M., Kiladis, G.N., 1999. Convectively coupled equatorial waves: Analysis of clouds and temperature in the wavenumber–frequency domain. Journal of the Atmospheric Sciences 56, 374–399.

Wu, L., Takahashi, M., 2018. Contributions of tropical waves to tropical cyclone genesis over the western North Pacific. Clim Dyn 50, 4635–4649. https://doi.org/10.1007/s00382-017-3895-3

Wu, L., Wen, Z., Wu, R., 2015a. Influence of the monsoon trough on westward-propagating tropical waves over the western North Pacific. Part I: Observations. Journal of Climate 28, 7108–7127.

Wu, L., Wen, Z., Wu, R., 2015b. Influence of the monsoon trough on westward-propagating tropical waves over the western North Pacific. Part II: Energetics and numerical experiments. Journal of Climate 28, 9332–9349.

Xie, F., Zhang, J., Sang, W., Li, Y., Qi, Y., Sun, C., Li, Y., Shu, J., 2017. Delayed effect of Arctic stratospheric ozone on tropical rainfall: The effect of ASO on tropical rainfall. Atmos. Sci. Lett. 18, 409–416. https://doi.org/10.1002/asl.783

Yang, G.-Y., Methven, J., Woolnough, S., Hodges, K., Hoskins, B., 2018. Linking African Easterly Wave Activity with Equatorial Waves and the Influence of Rossby Waves from the Southern Hemisphere. Journal of the Atmospheric

Sciences 75, 1783–1809. https://doi.org/10.1175/JAS-D-17-0184.1

Ying, Y., Zhang, F., 2017. Practical and Intrinsic Predictability of Multiscale Weather and Convectively Coupled Equatorial Waves during the Active Phase of an MJO. Journal of the Atmospheric Sciences 74, 3771–3785. https://doi.org/10.1175/JAS-D-17-0157.1

Zhang, L., Karnauskas, K.B., Weiss, J.B., Polvani, L.M., 2018. Observational evidence of the downstream impact on tropical rainfall from stratospheric Kelvin waves. Clim Dyn 50, 3775–3782. https://doi.org/10.1007/s00382-017-3844-1

Zschenderlein, P., Fragkoulidis, G., Fink, A.H., Wirth, V., 2018. Large-scale Rossby wave and synoptic-scale dynamic analyses of the unusually late 2016 heatwave over Europe: Large-scale Rossby wave and synoptic-scale dynamic analyses of the unusually late 2016 heatwave over Europe. Weather 73, 275–283. https://doi.org/10.1002/wea.3278